ROYAL SOCIETY OPEN SCIENCE

rsos.royalsocietypublishing.org

Research

Cite this article: Hou C, Liu W. 2018 One-step synthesis of OH-TiO_2/$TiOF_2$ nanohybrids and their enhanced solar light photocatalytic performance. *R. Soc. open sci.* **5**: 172005. http://dx.doi.org/10.1098/rsos.172005

Received: 26 November 2017
Accepted: 1 May 2018

Subject Category:
Chemistry

Subject Areas:
photochemistry/environmental chemistry

Keywords:
$TiOF_2$, OH-TiO_2/$TiOF_2$, MB, solar light, TiO_2, network

Author for correspondence:
Chentao Hou
e-mail: houct@xust.edu.cn

This article has been edited by the Royal Society of Chemistry, including the commissioning, peer review process and editorial aspects up to the point of acceptance.

Electronic supplementary material is available online at https://dx.doi.org/10.6084/m9.figshare.c.4106117.

THE ROYAL SOCIETY PUBLISHING

One-step synthesis of OH-TiO_2/$TiOF_2$ nanohybrids and their enhanced solar light photocatalytic performance

Chentao Hou and Wenli Liu

College of Geology and Environment, Xi'an University of Science and Technology, Xi'an 710054, People's Republic of China

CH, 0000-0002-3295-3012

TiO_2/$TiOF_2$ nanohybrids were quickly synthesized through a hydrothermal process using titanium n-butoxide (TBOT), ethanol (C_2H_5OH) and hydrofluoric acid as precursors. The prepared nanohybrids underwent additional NaOH treatment (OH-TiO_2/$TiOF_2$) to enhance their photocatalytic performance. In this paper, the mechanism of NaOH affecting the pathway of transformation from TBOT (Ti precursor) to TiO_2 nanosheets was discussed. The synthesized TiO_2/$TiOF_2$ and OH-TiO_2/$TiOF_2$ were characterized by field emission scanning electron microscopy (FE-SEM), high-resolution transmission electron microscopy (HRTEM), X-ray diffraction pattern (XRD), Fourier infrared spectroscopic analysis (FT-IR), Photoluminescence (PL) emission spectra and UV–visible diffuse reflection spectra (UV–vis DRS). The photocatalytic activity and stability of synthesized samples were evaluated by degradation of methylene blue (MB) under the simulated solar light. The results showed that a larger ratio of TiO_2 to $TiOF_2$ in TiO_2/$TiOF_2$ and OH-TiO_2/$TiOF_2$ nanohybrids could allow for even higher MB conversion compared with only TiO_2 nanosheets. NaOH treatment can wash off the F ions from $TiOF_2$ and induce this larger ratio. The highest efficiency of MB removal was just above 90% in 1 h. Lower electron–hole pairs recombination rate is the dominant factor that induces the photocatalytic performance enhancement of TiO_2/$TiOF_2$ nanohybrids. The synthesized OH-TiO_2/$TiOF_2$ nanohybrids exhibit great potential in the abatement of organic pollutants.

1. Introduction

As one of the most important materials, TiO_2 has been widely used as a promising catalyst due to its lack of toxicity, high stability and easy preparation. However, it has intrinsic

faults of a wide energy band gap (3.1–3.2 eV, meaning it only responds to UV light) and high electron–hole recombination, which hinders its use under solar or visible light [1–4]. Many studies examining TiO_2 has been devoted to reducing its energy band gap or photoelectron–hole separation [5–11].

Recently, Wen *et al.* [12] proposed a new visible light-driven $TiOF_2$ photocatalyst for H_2 evolution. Furthermore, Wang *et al.* [13] discovered a type of $TiOF_2$ photocatalyst that possesses proper activity and strong durability in photocatalytic degradation of rhodamine B and 4-chlorophenol under visible light, although its photocatalytic performance is not ideal. Heterostructured photocatalysts have attracted increasing attention during the past few years. The electronic assembling of different nanomaterials possessing dissimilar crystal structure and band edge positions allows the complete utilization of incident photons, while in-built electric fields at the interface assist effective charge carrier separation and induce excellent performance in terms of photocatalytic activity [5–11]. However, only a few investigations on the $TiO_2/TiOF_2$ nanocomposites with heterostructures have been performed so far. Zhao *et al.* [14] reported on a Pd@$TiO_2/TiOF_2$ photocatalyst made of TiO_2 shell and $TiOF_2$ core (labelled as $TiO_2/TiOF_2$) and further improved its performance by loading Pd nanoparticles onto the surfaces of $TiO_2/TiOF_2$ heterostructure, although its synthesis process is complex.

Among the typical synthesis methods, titanium (IV) butoxide and hydrofluoric acid (HF) are the most common precursors to provide anatase TiO_2 nanosheets with exposed facets [15–22]. In these papers, $TiOF_2$ was sometimes characterized by X-ray diffraction with a peak at $2\theta = 23.9°$, which occurs independently of the main (101) peak of anatase TiO_2 [17–22]. Almost all of these studies noted that $TiOF_2$ is the intermediate compound during the transformation of Ti^{4+} to titanium nanosheets (TiO_2) and aimed to suppress its appearance to obtain pure TiO_2 nanosheets [17–22]. A few of these studies paid attention to the photocatalytic activity of $TiOF_2$ or $TiO_2/TiOF_2$ systems, which performed more poorly when compared with (001)TiO_2 under UV or solar light [20–22]. For example, Lv *et al*. found that when $TiOF_2$ was calcined at 300°C, anatase TiO_2 and $TiOF_2$ were both observed, although the $TiOF_2$ and $TiO_2/TiOF_2$ samples showed poor photocatalytic activity compared with (001) TiO_2 under UV light for reactive brilliant red X3B [20]. Huang *et al*. also found that $TiOF_2$ has poor photocatalytic performance, although the performances of $TiO_2/TiOF_2$ systems were enhanced with an increased proportion of TiO_2 [21]. Yua *et al*. discussed the appearance of $TiOF_2$ and TiO_2 under different F/Ti atomic molar ratios, although they aimed to find the optimal ratios of exposed (101) and (001) facets of TiO_2. However, they did not mention the role of $TiOF_2$ in the $TiO_2/TiOF_2$ system [22]. Zhang *et al*. found that the mixture of (001)TiO_2 and $TiOF_2$ showed better photocatalytic activity for Rhodamine B (RhB) under simulated sunlight when they studied the reaction products of titanium butoxide and hydrogen fluoride. However, this did not show such good performance on MB for a reaction time as long as 10 h [23].

Alkali modification of catalysts has also been proven to be an effective way to enhance the photoactivity with methane dehydroaromatization, cumene cracking and CO oxidation [23–27]. For example, Han *et al*. found that alkali modification could form more hydroxyl groups on Au catalysts to enhance their catalytic activity [24]. Alkali-modified ZSM-5 zeolite also showed enhanced catalytic performance due to the formation of additional mesopores and the improvement in mass transfer and reaction kinetics [25,26]. NaOH-modified Pt/TiO_2 also showed enhanced performance in terms of the oxidation of formaldehyde under room temperature [27]. These studies have encouraged the modification of $TiO_2/TiOF_2$ by NaOH to enhance its catalytic performance.

In this study, $TiO_2/TiOF_2$ nanohybrids were synthesized and (001) TiO_2 was obtained through NaOH washing to remove the surface fluorine ions. NaOH was also used to modify the $TiO_2/TiOF_2$ nanohybrids to enhance their performance. This has not been investigated before. $TiO_2/TiOF_2$ nanohybrids even showed superior catalytic photoactivity towards methylene blue (MB) degradation under simulated sunlight for the first time. The possible mechanism of the $TiO_2/TiOF_2$ system in enhancing photocatalytic performance was also discussed.

2. Material and methods

2.1. Materials

Tetrabutyl titanite (TBOT) was purchased from Fu Chen Chemical Reagent Factory, Tianjin, China. HF was purchased from Xilong Chemical Industry Co Ltd, Sichuan, China. Sodium hydroxide (NaOH) and ethanol (C_2H_5OH) were purchased from Fuyu Fine Chemical Co., Ltd. Tianjin, China. Terephthalic acid, potassium iodide and p-benzoquinone were purchased from Shanghai Macklin Biochemical Co., Ltd.,

Shanghai, China. All reagents were A.R. grade and used without further purification. Ultra-pure water (18.2 MΩ•cm) was used as the water in all experiments.

2.2. Synthesis of $TiO_2/TiOF_2$ nanohybrids

A total of 15.2 ml of ethanol was added into 17.6 ml of TBOT, which was named solution A. Another 15.2 ml of ethanol and 5 ml of HF were added into 90 ml of ultra-pure water, which was named solution B. Solution A was dropped into solution B under medium-speed magnetic stirring at room temperature for 1.5 h to obtain a faint yellow sol. After this, the sol was transferred into a 200-ml Teflon-lined stainless steel autoclave. The autoclave was placed into an oven, which was maintained at 100°C for 0.5, 1, 1.5 and 2 h before being cooled to room temperature naturally to obtain a white precipitate. Ultra-pure water and C_2H_5OH were used to wash the precipitates several times to reach a pH of 7, before the precipitates were dried at a temperature of 100°C. The prepared samples were denoted as S0.5, S1, S1.5 and S2. The samples were then dispersed in 80 ml of 5 M NaOH solution for 30 min, before being washed with ultra-pure water and C_2H_5OH to reach a pH of 7. Finally, these samples were dried at 100°C for 12 h. The prepared samples were denoted as OH-S0.5, OH-S1, OH-S1.5 and OH-S2.

2.3. Characterization

The crystal structure was analysed by a XD-2 X-ray diffractometer (Beijing Purkinje, China) with Cu-Kα radiation. The morphology was examined by FE-SEM (JEOL JSM6700, Japan) equipped with EDS to probe elemental analysis and high-resolution transmission electron microscopy (HRTEM; Tecnai G2 F20, FEI, USA) using an accelerating voltage of 200 kV. Specific surface area and porosimetry were measured using Micromeritic TriStar II 3020 micrometrics (Micromeritics, USA), and the Brunauer–Emmett–Teller (BET) method was used to calculate the surface area (S_{BET}). Fourier transform infrared (FT-IR) spectra were recorded using a TENSOR27 (Bruker, Germany). The optical properties were determined by UV–vis diffuse reflectance spectroscopy (UV–vis DRS; Shimadzu 2600, Japan). Photoluminescence (PL) emission spectra were measured at room temperature with a fluorescence spectrophotometer (Hitachi F-2700, Japan) using a 325-nm line with an Xe lamp. X-ray photoelectron spectroscopy (XPS) took place under an ultra-high vacuum (10 Pa) at a pass energy of 100 eV on a Escalab 250 Xi system (ThermoFisher, USA) equipped with a dual X-ray source by using a Al K Alpha anode and a hemispherical energy analyser. All binding energies were calibrated with contaminant carbon (C1 s = 284.6 eV) as a reference.

2.4. Photocatalytic experiments

Photocatalytic activity was measured by degradation of MB. A total of 0.015 g of the catalyst was dispersed in a 150-ml double-layered quartz reactor containing 100 ml of a 10.0 mg l^{-1} MB solution. Cooling water was introduced into the interlayer of the quartz reactor to maintain the solution at room temperature. A Jiguang-300 W Xe lamp (simulating solar light) was located 30 cm away from the MB solution. A JB-420 cutoff filter was chosen to filter off light less than 420 nm to simulate visible light. The solution was magnetically stirred for 0.5 h in the dark to obtain the adsorption–desorption equilibrium, before the Xe lamp was turned on to start the degradation. At time intervals of 0.5 h, about 4.0 ml of the solution was extracted and centrifuged at a speed of 10 000 r.p.m. to remove catalysts. After this, the MB concentration was analysed with a Purkinje UV1901 UV–vis spectrophotometer at 665 nm. The photocatalyst was separated from the MB solution, before another run was started to investigate the durability of catalysts.

2.5. Radical-scavenging experiments

Radical-scavenging experiments were performed to ascertain the main active species in the photocatalytic process. Terephthalic acid (3 mmol l^{-1}), potassium iodide (3 mmol l^{-1}) and p-benzoquinone (3 mmol l^{-1}) were added to a mixed solution containing 15 mg of OH-TiO_2 and 100 ml of 10 mg l^{-1} of MB solution, respectively, while MB was degraded as a control.

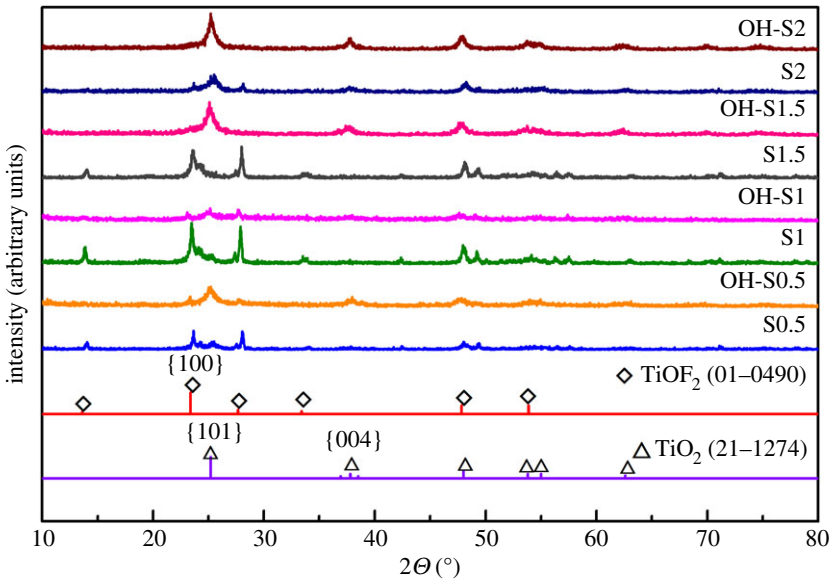

Figure 1. XRD patterns of prepared samples of S0.5, S1, S1.5, S2, OH-S0.5, OH-S1, OH-S1.5 and OH-S2.

3. Results

3.1. The formation mechanism of $TiOF_2$, $TiO_2/TiOF_2$ and TiO_2

The XRD patterns of the prepared samples were obtained under different experimental conditions (figure 1). All S0.5, S1, S1.5 and S2 samples showed diffraction peaks at 23.42° for $TiOF_2$ (100) facet and at 25.3° for TiO_2 (101) facet, indicating that the $TiOF_2$ (JCPDS No. 01–0049) and anatase TiO_2 (JCPDS No. 21–1272) phases coexist. Therefore, the S0.5, S1 and S1.5 samples are $TiO_2/TiOF_2$ nanohybrids. It also can be seen that with a longer reaction time, the ratio of peak height of (100) for $TiOF_2$ and TiO_2 for (101) changed from 0.44 to 4.4–4.5 and then to 0.55. This indicates that TiO_2 existed at the beginning, before the level decreased and was dominated by other compounds, then appeared and dominated again. This result is consistent with previous research [22]. After being washed with NaOH, the peak at 23.42° for (100) facet of $TiOF_2$ decreased and the peak at 25.3° for TiO_2 (101) facet increased, indicating an increase in the $TiO_2/TiOF_2$ ratio with a longer reaction time. For OH-S1.5 and OH-S2, the peak at 25.3° for TiO_2 (101) facet increased, indicating an increase in $TiO_2/TiOF_2$ ratio with a longer reaction time. For OH-S1.5 and OH-S2, the $TiOF_2$ complex disappeared. The (004) facet of TiO_2 even emerged, which was named the (001)-faceted TiO_2 existence. It seems that OH in NaOH can exchange with F ions in the crystal lattice of $TiOF_2$, converting it into (001)-faceted TiO_2 nanosheets [14,18,22].

In summary, the chemical reactions of the formation of titanium nanosheets can be proposed. The first step is the hydrolysis reaction. The reaction of TBOT to form $Ti(OH)_4$ is shown in equation (3.1). Secondly, in equation (3.2), $Ti(OH)_4$ can react with HF to produce $TiOF_2$ through water condensation [28,29]. Finally, $TiOF_2$ can react with NaOH to form TiO_2, as shown in equation (3.3) [30].

$$Ti(OC_4H_9)_4 + H_2O \rightarrow Ti(OH)_4 + 4(C_4H_9OH) \quad \text{(hydrolysis)}, \tag{3.1}$$

$$Ti(OH)_4 + 2HF \rightarrow TiOF_2 + 3H_2O \quad \text{(water condensation)} \tag{3.2}$$

and

$$TiOF_2 + 2NaOH \rightarrow TiO_2(\text{anatase}) + 2NaF + H_2O \quad (\textit{in situ}\ \text{transformation}). \tag{3.3}$$

This study provides a simple conversion method of $TiOF_2$ to TiO_2 in addition to the calcination of $TiOF_2$ [20,21].

3.2. Morphology analysis

The morphology of the prepared samples was characterized by FE-SEM and high-resolution transmission electron microscope (HRTEM) in figures 2 and 3. The SEM and HRTEM images shown in figure 2 and figure 3*a*,*b*, respectively, were used to obtain the morphology of photocatalysts. The S0.5, S1 and S1.5 samples exhibit mixtures of two types of crystals connected together, which correspond to $TiOF_2$ and TiO_2 according to the XRD results in figure 1. By contrast, S2 shows a nano-network look,

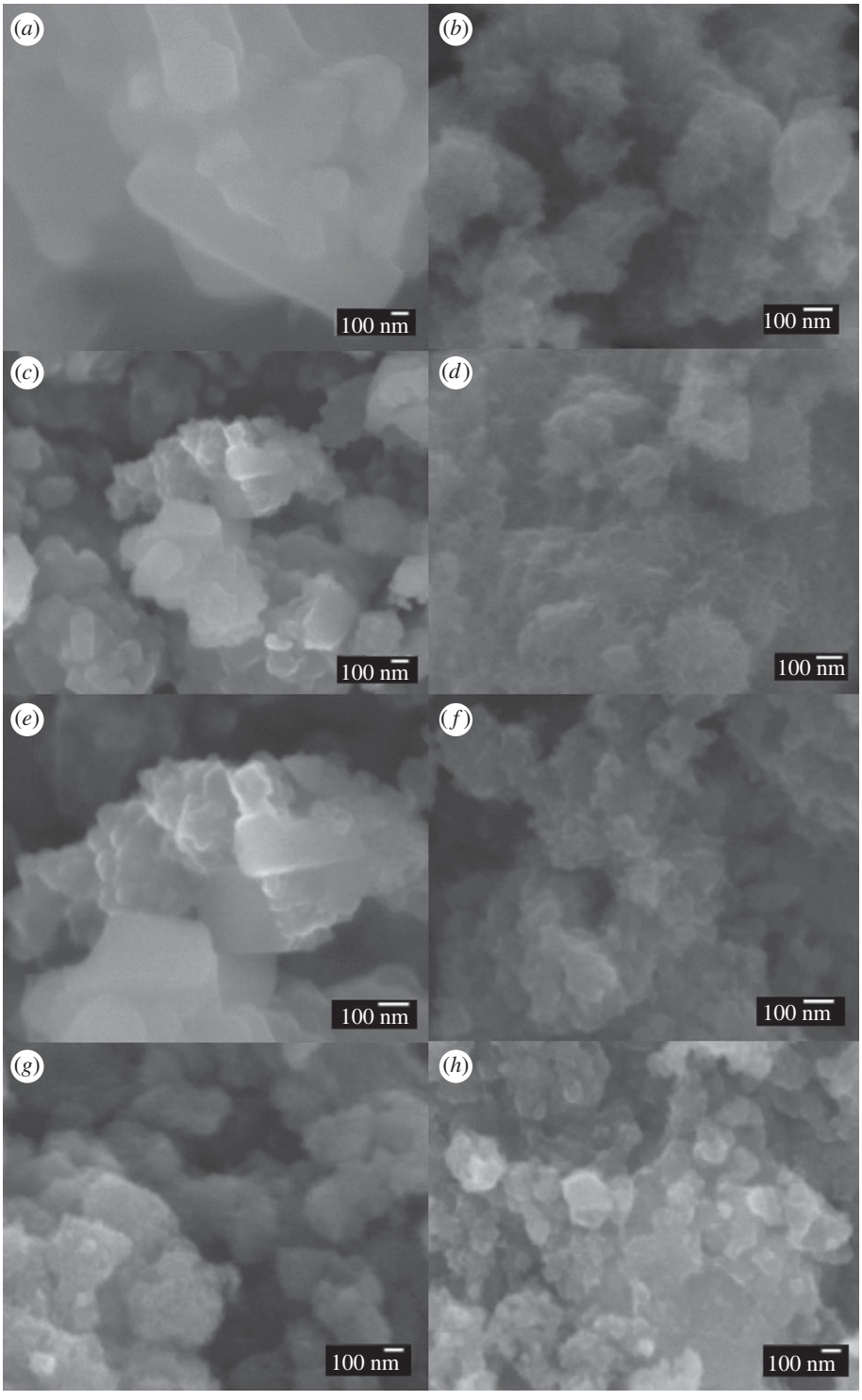

Figure 2. SEM of (*a*) S0.5, (*b*) OH-S0.5, (*c*) S1, (*d*) OH-S1, (*e*) S1.5, (*f*) OH-S1.5, (*g*) S2 and (*h*) OH-S2.

corresponding to TiO_2. The OH-S0.5, OH-S1 and OH-S1.5 samples exhibited a nano-network look after reaction with NaOH, permitting light scattering inside the catalyst and enhancing its absorption in light.

As also can be seen in figure 3*c*,*d*, the lattice fringes of 0.19 nm, 0.235 nm and 0.352 nm were assigned to the (200) (001) and (101) planes of TiO_2, respectively [18,22,30]. The lattice fringes of 0.38 nm were assigned to the (100) planes of $TiOF_2$ [12,13]. This also indicates that the S0.5 and OH-S0.5 samples are nanohybrids of TiO_2 and $TiOF_2$, which is consistent with the XRD and SEM results. The EDS spectrum (figure 3*e*) shows that OH-S0.5 consists of Ti, O and F elements. The uniform distribution of Ti, O and F can be seen from the EDS elemental mapping (figure 3*f*–*h*), which suggests the successful formation of a heterojunction.

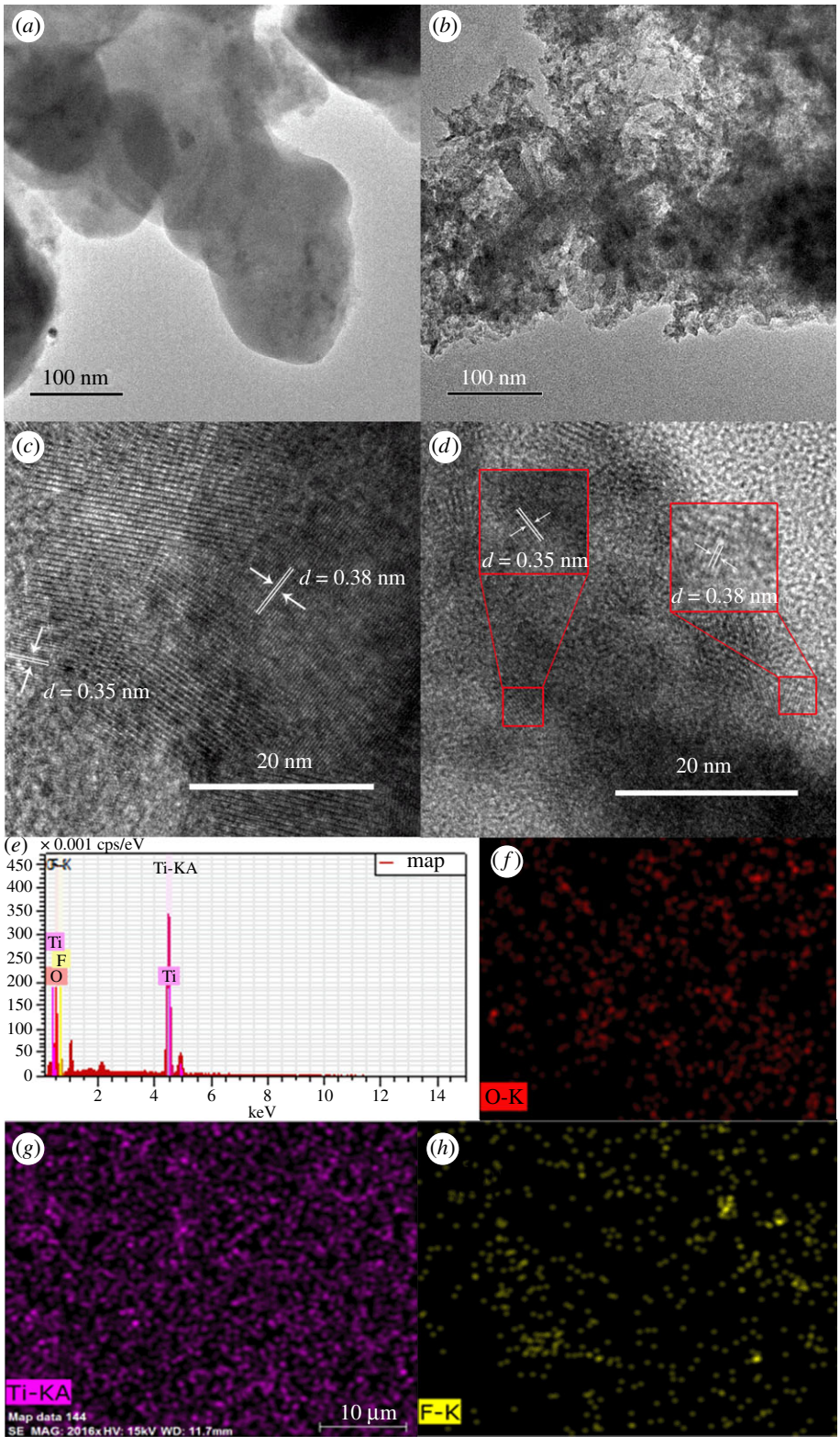

Figure 3. HRTEM and EDS spectra of S0.5 and OH-S0.5 samples: (*a*) TEM of S0.5, (*b*) TEM of OH-S0.5, (*c*) HRTEM of S0.5, (*d*) HRTEM of OH-S0.5, (*e*) EDS of OH-S0.5, and (*f–h*) EDS elemental mapping of OH-S0.5.

3.3. S_{BET} and pore-size distribution

Figure 4 shows the nitrogen adsorption–desorption isotherms and the corresponding pore-size distribution curves of prepared samples. Considering the BET data in electronic supplementary material,

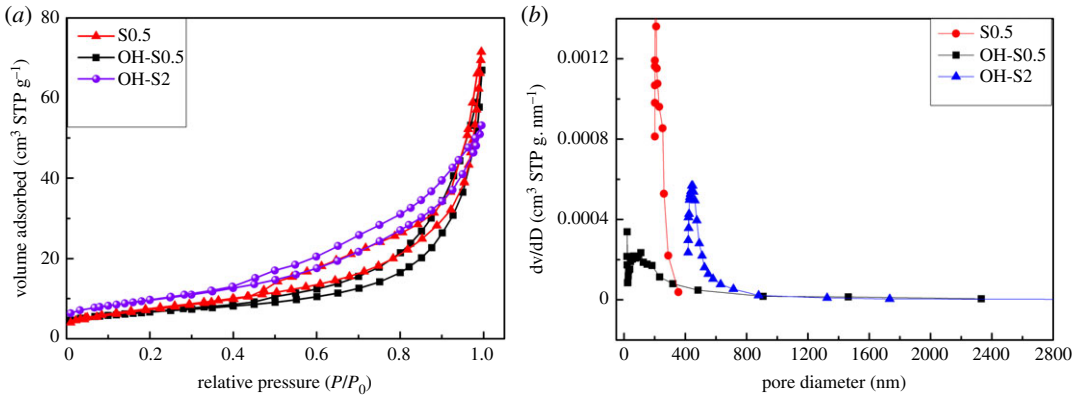

Figure 4. (*a*) Nitrogen adsorption–desorption isotherms and (*b*) the corresponding pore-size distribution curves of S0.5, OH-S0.5 and OH-S2.

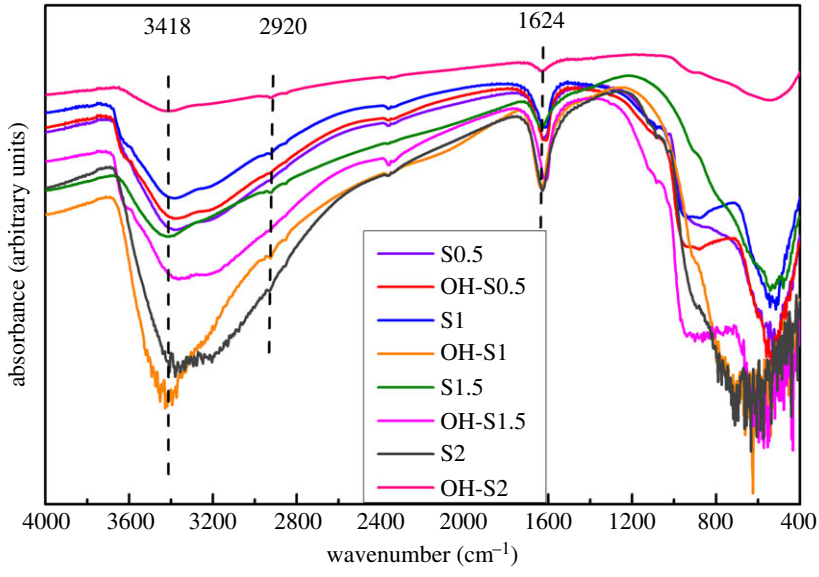

Figure 5. FT-IR spectra of S0.5, S1, S1.5, S2, OH-S0.5, OH-S1, OH-S1.5 and OH-S2.

table S1, the S_{BET} and pore volume of S2 can reach as high as 59.3 $m^2 \cdot g^{-1}$ with a pore size of 62.5 nm, while the S_{BET} of S0.5 and OH-S0.5 are significantly lower with values of 23.6 and 27.21 $m^2 \cdot g^{-1}$, respectively, and pore sizes of 122.6 and 14.49 nm, respectively. After NaOH washing, the S_{BET} of OH-S0.5 was a bit lower than that of S0.5, but the pore size was dramatically decreased.

3.4. FT-IR analysis

As shown in figure 5, broad absorptions centered around 3418 and 2920 cm^{-1} as well as the weak sharp absorption band centred around 1624 cm^{-1} were attributed to the hydroxyl free radicals, associated hydrogen bonds and absorption water. The OH and water in all NaOH-reacted samples are all stronger than those modified before, with the exception of OH-S2. For the OH-S2 sample, the OH from the broad absorptions centred around 3418, 2920 and 1624 cm^{-1} sharply decreased. According to XRD results, the S2 and NaOH-reacted samples are all $TiO_2/TiOF_2$ nanohybrids, except OH-S2. It was concluded that $TiO_2/TiOF_2$ nanohybrids can adsorb more OH to enhance photocatalytic performance [31–37].

3.5. XPS analysis

In figure 6, XPS survey spectra of the prepared samples of S0.5 and OH-S0.5 are presented. As observed in figure 6*a*, all the samples have sharp photoelectron peaks at binding energies of Ti 2p, O 1s and F 1s. Another sharp photoelectron peak appears in all samples at the binding energy (BE) of 285 eV (C 1s) due

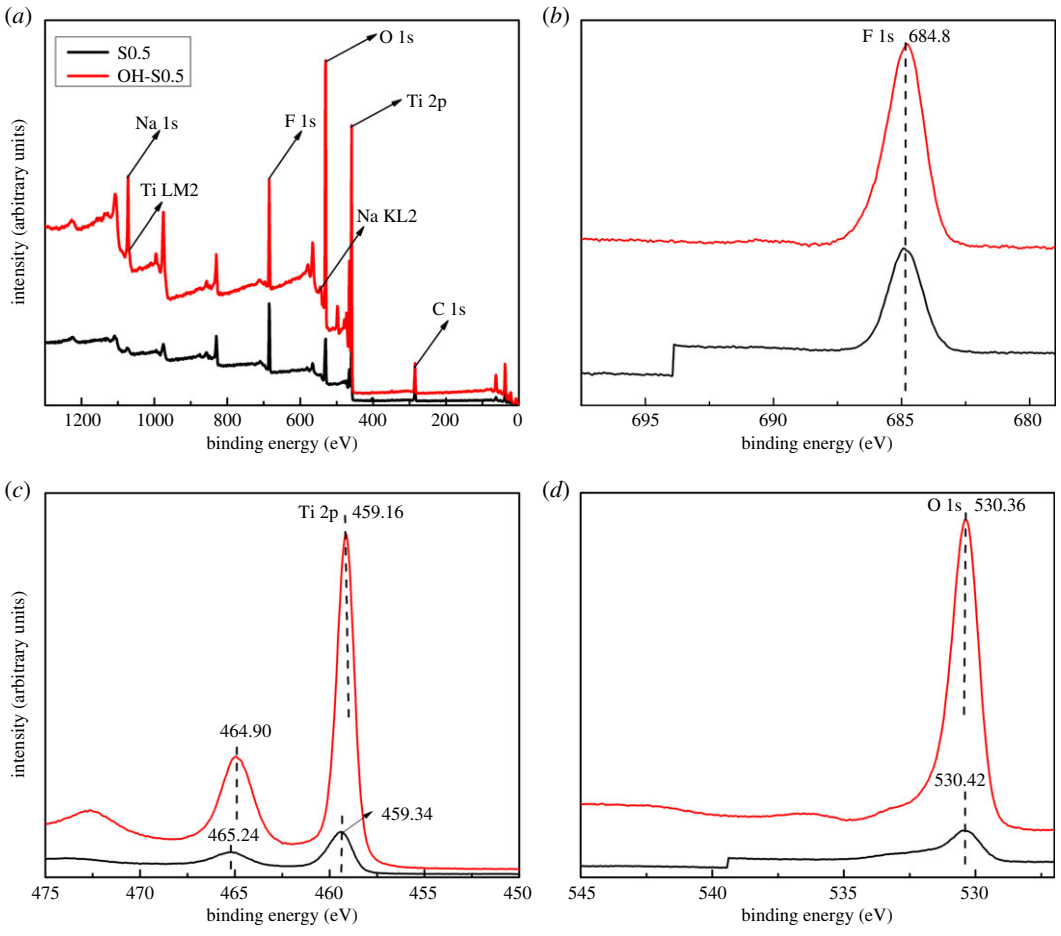

Figure 6. High-resolution XPS survey spectra for (*a*) all samples, (*b*) F 1s, (*c*) Ti 2p and (*d*) O 1s of the S0.5 and OH-S0.5 samples.

to the contamination of the XPS instrument itself [23,38–41]. The F 1s BE of 684.8 eV in this spectrum (figure 6*b*) corresponds to that of F adsorbed on TiO_2, while there was no sign of F ions in the lattice (BE = 688.5 eV) [38,39]. The measured binding energies of Ti 2p3/2 and Ti 2p1/2 (figure 6*c*) for S0.5 were 459.3 and 465.2 eV, respectively. The main sharp peaks of Ti 2p3/2 were assigned to Ti^{4+} in TiO_2 [23,39–41]. As compared to S0.5, the binding energies of OH-S0.5 shifted to 459.16 and 464.9 eV, respectively. One possible explanation is that TiO_2 is partially reduced into Ti^{3+} [23,41]. As $Ti^{3+}$is more hydrophilic than Ti^{4+}, oxygen and water molecules are easily adsorbed on the surface of TiO_2, which consequently facilitates the formation of surface OH groups. The measured BE of O 1s (figure 6*d*) was 530.42 eV, while this shifted to 530.36 eV in OH-S0.5. This can be explained by OH-S0.5 possibly having many oxygen vacancies that are generated at the interface of $TiO_2/TiOF_2$. Oxygen from the gas phase could dissociate and become adsorbed on such defects, thus resulting in a decrease in binding energies of O 1s to TiO_2 lattice oxygen (Ti−O−Ti) [23]. So it can be concluded that NaOH treatment can induce more surface OH groups and oxygen vacancies at the interface of $TiO_2/TiOF_2$, which would enhance the photocatalytic performance of $TiO_2/TiOF_2$ nanohybrids.

3.6. UV–vis DRS analysis

Figure 7 shows the UV–vis absorption spectroscopy and band gap of the prepared $TiO_2/TiOF_2$ nanohybrids and TiO_2 samples. It can be seen that S2 and OH-S0.5 have a greater increase in adsorption in both the range of UV and visible light compared with other samples. By contrast, they contain more TiO_2 compared to S0.5, which corresponds to the XRD results. While the OH-S2 sample has weaker adsorption than S2, it becomes TiO_2 after NaOH washing. Therefore, a larger ratio of $TiO_2/TiOF_2$ causes the stronger light adsorption. The band gaps of S2, OH-S2 and OH-S0.5 are 2.77, 3.05 and 3.12 eV, respectively, which are lower than that of P25 (3.2 eV). This indicates that they are more easily excited by visible light.

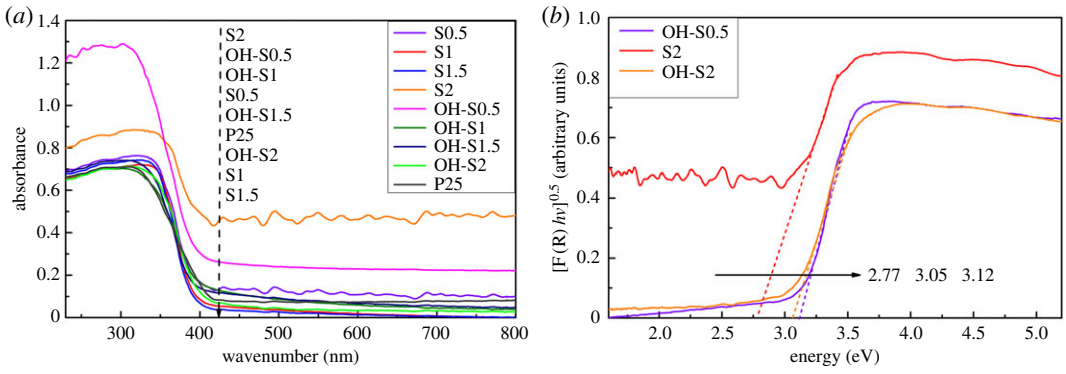

Figure 7. (*a*) UV–vis absorption spectroscopy and (*b*) band gap of prepared TiO_2 /$TiOF_2$ nanohybrids and TiO_2 samples.

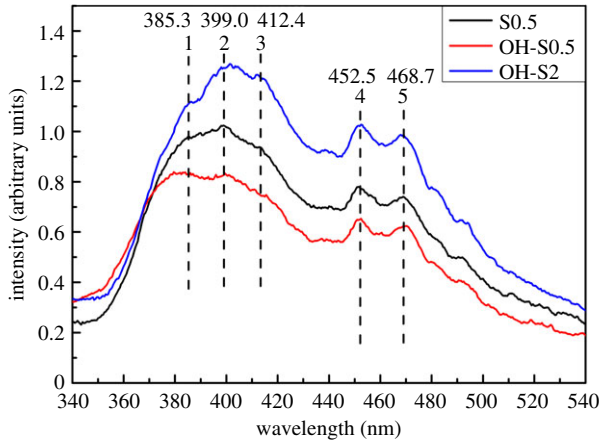

Figure 8. PL spectra of S0.5, OH-S0.5 and OH-S2 samples.

3.7. PL analysis

PL emission spectra were used to investigate the efficiency of charge carrier trapping, immigration and transfer as well as to understand the fate of electron hole pairs in catalysts (figure 8). Six peaks were observed in the spectra. The broad emission bands centred at 385.3 nm (peak 1), 399.0 nm (peak 2) and 412.4 nm (peak 3) were ascribed to form the boundaries of exciton emission due to the trapping of free excitons by titanite groups near defects [42]. The long wavelength range of 452.5–468.7 nm (peaks 4 and 5) is attributed to the oxygen vacancy with two trapped electrons. Oxygen vacancy sites are important for the formation of superoxide (O_2•−) and hydroxyl (•OH) radicals for photocatalytic degradation. A lower PL intensity also indicates a lower recombination rate of electron–hole pairs and higher separation efficiency, thus representing higher photocatalytic activity [43].

3.8. Catalytic activities of TiO_2/$TiOF_2$ and TiO_2 photocatalysts

Figure 9*a* shows the solar light photocatalytic properties of the prepared samples and P25. Figures 9*a* and S1 showed that with 0.015 g/100 ml of catalysts, the decrease in MB was very small in the first 0.5 h in dark and in light without a catalyst, indicating that this decrease in MB was a photocatalytic process with all samples being activated in solar or visible light. It also shows that the S2 and OH-S0.5 samples can cause almost complete decomposition of MB in about 1.5 h with better photocatalytic performance than all of the other samples. By contrast, P25 performed poorly compared to TiO_2/$TiOF_2$ and (001) TiO_2. All NaOH-treated nanohybrids showed higher performance than untreated ones except the pure (001)-facet TiO_2 from S2.

The activity arrangement order was consistent with the TiO_2/$TiOF_2$ ratio. A larger ratio of TiO_2/$TiOF_2$ resulted in better photocatalytic activity. This result is consistent with Yua *et al.*'s research

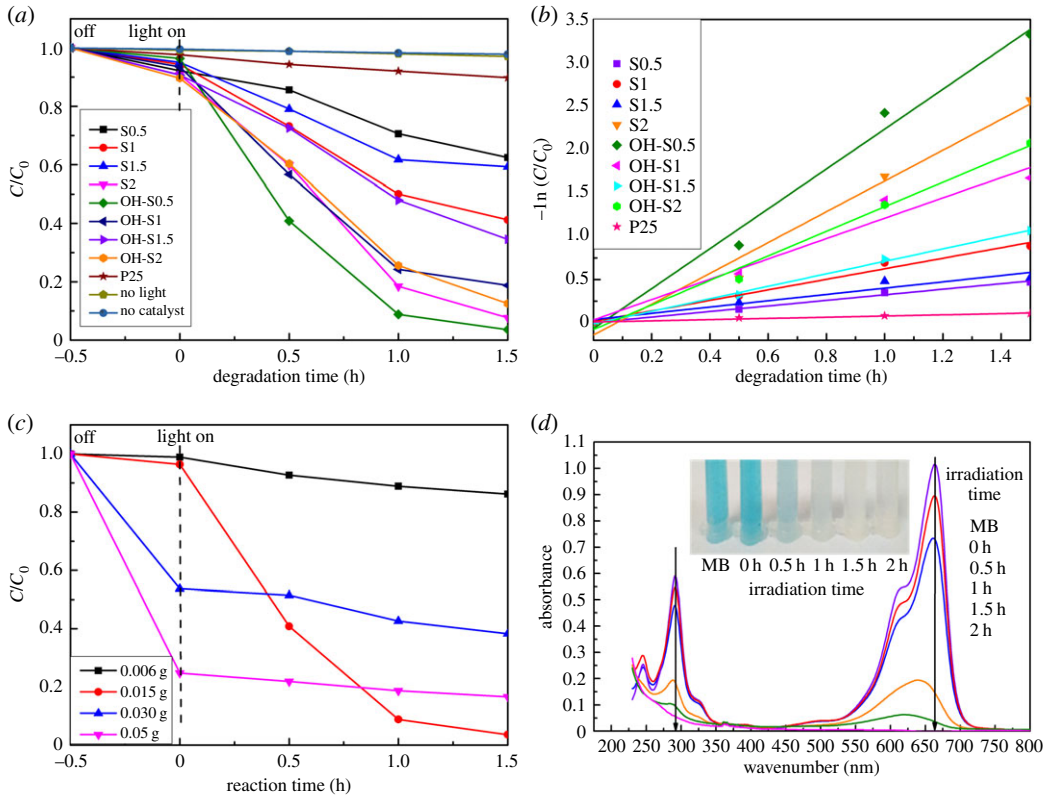

Figure 9. Solar light photocatalytic properties of the prepared samples, P25 and UV–vis spectra of MB with irradiation time: (*a*) comparison of solar light-sensitized degradation of MB in the suspension of samples; (*b*) the reaction rate of all samples; (*c*) the effect of different amounts of catalysts on the solar light photocatalytic properties of the prepared OH-S0.5 samples; and (*d*) UV–vis absorption spectral changes of MB with solar light irradiation time by OH-S0.5.

[22]. It can be explained by the better charge separation capability of the $TiOF_2$–TiO_2 mixed phase, which reduces the recombination rate of electron–hole pairs. However, a high amount of $TiOF_2$ phase in the TiO_2 nanosheets would decrease the photoactivity due to poor photoactivity of $TiOF_2$.

The reaction rate of all of the samples is shown in figure 9*b*. The data were fitted with the first-order reaction equation as follows:

$$\ln\left(\frac{C_0}{C}\right) = kt, \tag{3.4}$$

where t is the reaction time, C_0 is the concentration of RhB at time 0, C is the concentration of RhB at time t, and k is the reaction rate constant. Figure 9*b* shows that P25 had a rate constant of only 0.07 h^{-1}, indicating poor photocatalytic performance. The calculated rate constants are 1.4 and 2.3 h^{-1} for S2 and OH-S0.5, respectively. The OH-S0.5 sample shows the best performance among all the photocatalysts, with a degradation rate that is much higher than that of the P25, $TiO_2/TiOF_2$ and TiO_2 samples. This excellent performance could be mainly attributed to its stronger light adsorption and $TiO_2/TiOF_2$ combination.

The catalytic abilities of 0.006 g/100 ml, 0.030 g/100 ml and 0.050 g/100 ml (OH-S0.5) are also shown in figure 9*c*. For the catalytic amount of 0.015 g/100 ml, the photocatalytic degradation rate of MB was the strongest and had the best degradation effect (figure 9*c*). When the content of OH-S0.5 was increased, its adsorptive capacity increased but photocatalytic degradation performance decreased (figure 9*c*).

Figure 9*d* shows the UV–vis absorption spectral changes of the MB solution. According to previous research, the discoloration of MB can be caused in two ways: the oxidative degradation and the two-electron reduction to leuco-MB, which can be detected by the UV–vis absorption at 256 nm [44,45]. Figure 9*d* shows that there is a blue-shift from 665 to 625 nm with an absorbent peak emerging at 256 nm after the spectral change of MB with the irradiation time by OH-S0.5. This means that a reductive conversion to leuco-MB exists in the degradation path of MB.

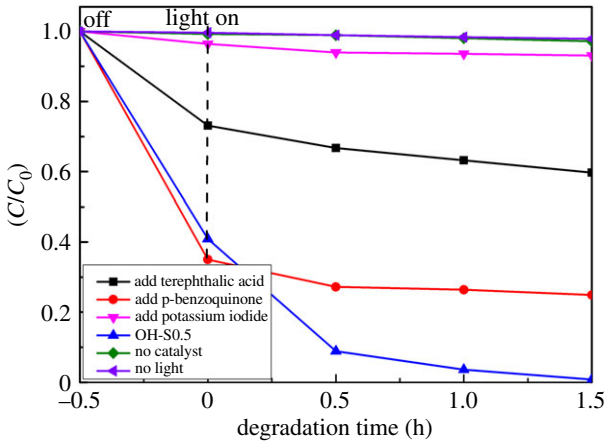

Figure 10. Photocatalytic degradation of MB in the presence of different scavengers over OH-S0.5 under simulated solar light irradiation.

3.9. Radical-scavenging experiments

Radical-scavenging experiments were performed to complete an in-depth study of the photocatalytic degradation mechanism. The reactive species were detected through trapping experiments of hydroxyl radicals (•OH), holes (h^+) and superoxide radical anions (O_2•−) by introducing terephthalic acid [46], potassium iodide [46] and p-benzoquinone [47]. Terephthalic acid can combine with the hydroxyl radicals (•OH), potassium iodide can combine with holes (h^+), and p-benzoquinone can combine with the superoxide radical (O_2•−), to decrease the activity of the catalyst [46,47]. The effects of a series of scavengers on the photocatalytic oxidation towards the MB dye over the photocatalysts are shown in figure 10. Under simulated sunlight illumination, the percentage of MB loss decreased most rapidly after the addition of potassium iodide, indicating h^+ was the main active species in the photocatalytic process. When terephthalic acid and p-benzoquinone were added, this also reduced activity, which implied that •OH and O_2•− radicals also played a role in the photooxidation of MB. The order of importance of the active species is h^+, •OH and O_2•−.

4. Discussion

$TiOF_2$ photoactivity was quite low, nearly 150 times lower than P25 in the X3B dye degradation experiment [36]. Lv *et al*. reported that surface fluorination can greatly enhance the photocatalytic activity of TiO_2 due to the formation of free •OH radicals, which are highly reactive [37]. In this research, a combination of TiO_2 and $TiOF_2$ demonstrated even higher photoactivity performance in MB degradation compared with the pure TiO_2 nanosheets. In order to further understand the reason for the enhanced photocatalytic performance, a possible mechanism of charge separation and transfer on the surface of $TiO_2/TiOF_2$ nanohybrids is proposed. The conduction band (E_c) and valence band (E_v) potentials of TiO_2 and $TiOF_2$ at the point of zero charge can be calculated by the following empirical equation [11,14,44]: $E_c = \chi - E_0 - 0.5\,E_g$, where E_c is the energy of the conduction band, X is the bulk Mulliken electronegativity of the compound, E_0 is the energy of free electrons on the hydrogen scale (about 4.5 eV), and E_g is the band gap energy of the semiconductor. The x-values for TiO_2 and $TiOF_2$ are approximately 5.8 and 7.3 eV, respectively. The energy gap (E_g) was estimated from the intercept of the tangent in the plots of $(\alpha h\nu)^{1/2}$ versus photon energy ($h\nu$), which is shown in figure 7*b*. The E_g of TiO_2 and $TiOF_2$ were evaluated to be 3.2 eV and 2.94 eV, respectively.

The position of the valence band edge (E_v) is determined by the following equation:

$$E_v = E_c + E_g. \tag{4.1}$$

The calculated E_c and E_v of TiO_2 and $TiOF_2$ are shown in the electronic supplementary material, table S2. The E_c edge potential of TiO_2 (–0.3 eV) is more active than that of $TiOF_2$ (1.5 eV). Hence, the photogenerated electrons on the TiO_2 surface have a strong capability for moving onto the surfaces of $TiOF_2$ via the interface transfer pathway. Similarly, photogenerated holes on the $TiOF_2$ surface migrate to TiO_2 under the driving force of the E_v edge potentials (figure 11). As a result, the electron–hole

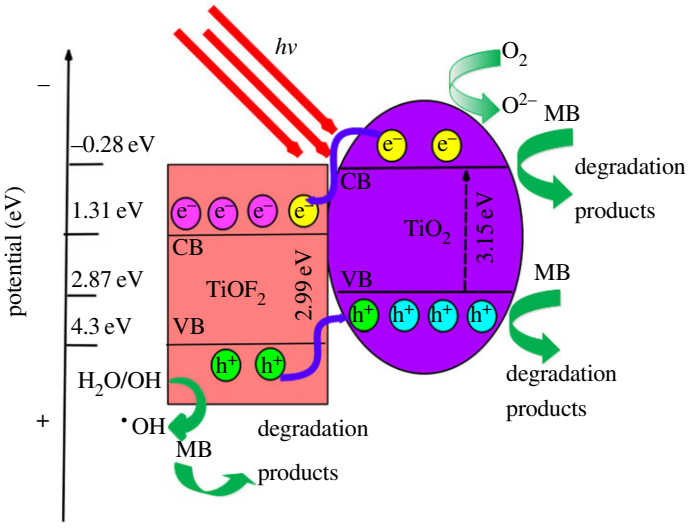

Figure 11. Schematic diagram for the conduction and valence bands of TiO_2 and $TiOF_2$, and the degradation route of MB under solar light irradiation.

recombination is reduced, which is consistent with PL analysis. Thus, under simulated solar light irradiation, more h^+ radicals can react with H_2O or OH^- to produce •OH, while more electrons can react with the dissolved oxygen molecules to yield superoxide radical anions (O_2•−) [48,49]. MB can also be decomposed by the holes directly [50]. Because the photocatalytic activity of TiO_2 is better than that of $TiOF_2$, a larger ratio of TiO_2 /$TiOF_2$ (S2 and OH-S0.5) results in better photocatalytic activity. NaOH treatment can induce more F ions being disconnected from the surface of $TiOF_2$, which means a larger ratio of $TiO_2/TiOF_2$ (XRD results). Furthermore, the presence of OH bonds on the surface of the photocatalyst (FT-IR analysis) and more oxygen vacancies (XPS and PL analysis) also induce the production of more •OH with enhancement of the photocatalytic performance. This can explain why NaOH-treated nanohybrids showed greater performance than untreated ones. OH-S0.5 showed the best photocatalytic activity, even better than S2; this may be attributed to its lower recombination rate of electron–hole pairs introducing more h^+, and more Ti^{4+} being reduced into Ti^{3+}, because its OH, S_{BET} and absorption of light are not the largest according to FT-IR and UV–vis DRS analysis. So a lower electron–hole pairs recombination rate is the dominant factor that induces the photocatalytic performance enhancement of $TiO_2/TiOF_2$ nanohybrids. This was in accord with the radical-scavenging experiments.

5. Conclusion

In summary, an easy one-step hydrothermal route to synthesize $TiO_2/TiOF_2$ and OH-$TiO_2/TiOF_2$ hybrids has been demonstrated. The introduction of NaOH facilitated the conversion from $TiOF_2/TiO_2$ and induced a network structure. The prepared $TiO_2/TiOF_2$, especially the OH-$TiO_2/TiOF_2$ nanocomposite, exhibited excellent activity towards the degradation of MB under simulated sunlight irradiation. A larger ratio of $TiO_2/TiOF_2$ in $TiO_2/TiOF_2$ and OH-$TiO_2/TiOF_2$ nanohybrids could enable better performance. NaOH treatment can wash off the F ions from $TiOF_2$ and induce this larger ratio. The highest efficiency of MB removal was just above 90% in 1 h. A lower electron–hole pairs recombination rate is the dominant factor that induces the photocatalytic performance enhancement of $TiO_2/TiOF_2$ nanohybrids.

Therefore, this work opens an avenue to efficiently synthesize $TiO_2/TiOF_2$ through a one-step nanocomposite for the removal of organic pollutants.

Data accessibility. The datasets supporting this article have been uploaded as part of the electronic supplementary material.

Authors' contributions. H.C. designed the experiments, analysed and interpreted the data and wrote the article. L.W. carried out the experiments, helped analyse and interpret the data and drew the figures. Both authors are accountable for all aspects of the work in ensuring that questions related to the accuracy or integrity of any part of the work are appropriately investigated and resolved. Both authors also approved the article to be published.

Competing interests. We have no competing interests.
Funding. Financial support was provided by Shaanxi Key Industrial Projects (2014GY2-07) and the Shaanxi Province Education Department Science and Technology Research Plan (15JK1460).

References

1. Chen X, Mao SS. 2007 Titanium dioxide nanomaterials: synthesis; properties; modifications; and applications. *Chem. Rev.* **107**, 2891–2959. (doi:10.1021/cr0500535)
2. Nunes D, Pimentel A, Santos L, Barquinha P, Fortunato E, Martins R. 2017 Photocatalytic TiO_2 nanorod spheres and arrays compatible with flexible applications. *Catalyst* **7**, 60. (doi:10.3390/catal7020060)
3. Li H, Bian Z, Zhu J, Huo Y, Li H, Lu Y. 2007 Mesoporous Au/TiO_2 nanocomposites with enhanced photocatalytic activity. *J. Am. Chem. Soc.* **129**, 4538–4539. (doi:10.1021/ja069113u)
4. Rashed MN, Eltaher MA, Abdou ANA. 2017 Adsorption and photocatalysis for methyl orange and Cd removal from wastewater using TiO_2/sewage sludge-based activated carbon nanocomposites. *R. Soc. open sci.* **4**, 170834. (doi:10.1098/rsos.170834)
5. Girish Kumar S, Koteswara Rao KSR. 2017 Comparison of modification strategies towards enhanced charge carrier separation and photocatalytic degradation activity of metal oxide semiconductors (TiO_2, WO_3 and ZnO). *Appl. Surf. Sci.* **391**, 124–148. (doi:10.1016/j.apsusc.2016.07.081)
6. Low J, Cheng B, Yu J. 2017 Surface modification and enhanced photocatalytic CO_2 reduction performance of TiO_2: a review. *Appl. Surf. Sci.* **392**, 658–686. (doi:10.1016/j.apsusc.2016.09.093)
7. Yu T, Liu L, Yang F. 2017 Heterojunction between anodic TiO_2/g-C_3N_4 and cathodic WO_3/W nano-catalysts for coupled pollutant removal in a self-biased system. *Chin. J. Catal.* **38**, 270–277. (doi:10.1016/S1872-2067(16)62556-1)
8. Li G, Wu L, Li F, Xu P, Zhang D, Li H. 2013 Photoelectrocatalytic degradation of organic pollutants via a CdS quantum dots enhanced TiO_2 nanotube array electrode under visible light irradiation. *Nanoscale* **5**, 2118–2125. (doi:10.1039/C3NR34253K)
9. Wang M, Sun L, Lin Z, Cai J, Xie K, Lin C. 2013 P–N heterojunction photoelectrodes composed of Cu_2O-loaded TiO_2 nanotube arrays with enhanced photoelectrochemical and photoelectrocatalytic activities. *Energy Environ. Sci.* **6**, 1211–1220. (doi:10.1039/C3EE24162A)
10. Zhou W, Yin Z, Du Y, Huang X, Zeng Z, Fan Z, Liu H, Wang J, Zhang H. 2013 Synthesis of few-layer MoS_2 nanosheet-coated TiO_2 nanobelt heterostructures for enhanced photocatalytic activities. *Small* **9**, 140–147. (doi:10.1002/smll.201201161)
11. Dong P, Cui E, Hou G, Guan R, Zhang Q. 2015 Synthesis and photocatalytic activity of Ag_3PO_4/$TiOF_2$ composites with enhanced stability. *Mater. Lett.* **143**, 20–23. (doi:10.1016/j.matlet.2014.12.063)
12. Wen CZ, Hu QH, Guo YN, Gong XQ, Qiao SZ, Yang HG. 2011 From titanium oxydifluoride ($TiOF_2$) to titania (TiO_2): phase transition and non-metal doping with enhanced photocatalytic hydrogen (H_2) evolution properties. *Chem. Commun.* **47**, 6138–6140. (doi:10.1039/C1CC10851D)
13. Wang J, Cao F, Bian Z, Leung MK, Li H. 2013 Ultrafine single-crystal $TiOF_2$ nanocubes with mesoporous structure; high activity and durability in visible light driven photocatalysis. *Nanoscale* **6**, 897–902. (doi:10.1039/C3NR04489K)
14. Zhao X, Wei G, Liu J, Wang Z, An C, Zhang J. 2016 Synthesis of heterostructured Pd@TiO_2/$TiOF_2$ nanohybrids with enhanced photocatalytic performance. *Mater. Res. Bull.* **80**, 337–343. (doi:10.1016/j.materresbull.2016.04.018)
15. Zhu S, Liang S, Gu Q, Xie L, Wang J, Ding Z, Liu P. 2012 Effect of Au supported TiO_2 with dominant exposed {001} facets on the visible-light photocatalytic activity. *Appl. Catal. B* **119–120**, 146–155. (doi:10.1016/j.apcatb.2012.02.020)
16. Yang XH, Li Z, Liu G, Xing J, Sun C, Yang HG, Li C. 2011 Ultra-thin anatase TiO_2 nanosheets dominated with {001} facets: thickness-controlled synthesis, growth mechanism and water-splitting properties. *CrystEngComm* **13**, 1378–1383. (doi:10.1039/c0ce00233j)
17. Wang Z, Huang B, Dai Y, Zhang X, Qin X, Li Z, Zheng Z, Cheng H, Guo L. 2012 Topotactic transformation of single-crystalline $TiOF_2$ nanocubes to ordered arranged 3D hierarchical TiO_2 nanoboxes. *CrystEngComm* **14**, 4578–4581. (doi:10.1039/C2CE25271F)
18. He Z, Wen L, Wang D, Xue Y, Lu Q, Wu C, Chen J, Song S. 2014 Photocatalytic reduction of CO_2 in aqueous solution on surface-fluorinated anatase TiO_2 nanosheets with exposed {001} facets. *Energy Fuels* **28**, 3982–3993. (doi:10.1021/ef500648k)
19. Peng JD, Lin H-H, Lee C-T, Tseng C-M, Suryanarayanan V, Vittal R, Ho K-C. 2016 Hierarchically assembled microspheres consisting of nanosheets of highlyexposed (001)-facets TiO_2 for dye-sensitized solar cells. *RSC Adv.* **6**, 14 178–14 191. (doi:10.1039/C5RA26307G)
20. Lv K, Yu J, Cui L, Chen S, Li M. 2011 Preparation of thermally stable anatase TiO_2 photocatalyst from $TiOF_2$ precursor and its photocatalytic activity. *J. Alloys Compd.* **509**, 4557–4562. (doi:10.1016/j.jallcom.2011.01.103)
21. Huang Z, Wang Z, Lv K, Zheng Y, Deng K. 2013 Transformation of $TiOF_2$ cube to a hollow nanobox assembly from anatase TiO_2 nanosheets with exposed {001} facets via solvothermal strategy. *ACS Appl. Mater. Interfaces* **5**, 8663–8669. (doi:10.1021/am4023048)
22. Yua JC-C, Nguyenb V-H, Lasekc J, Wu JCS. 2017 Titania nanosheet photocatalysts with dominantly exposed (001) reactive facets for photocatalytic NOx abatement. *Appl. Catal. B* **219**, 391–400. (doi:10.1016/j.apcatb.2017.07.077)
23. Zhang Y, Xia T, Shang M, Wallenmeyer P, Katelyn D, Peterson A, Murowchick J, Dong L, Chen X. 2014 Structural evolution from TiO_2 nanoparticles to nanosheets and their photocatalytic performance in hydrogen generationand environmental pollution removal. *RSC Adv.* **4**, 16 146–16 152. (doi:10.1039/c3ra48066f)
24. Han D-Q, Zhou C-Q, Yin H-M, Zhang D-J, Xu X-H. 2011 Reactivity of the alkaline pretreated nanoporous gold for the CO oxidation. *Catal. Lett.* **141**, 1026–1031. (doi:10.1007/s10562-011-0619-x)
25. Gopalakrishnan S, Zampieri A, Schwieger W. 2008 Mesoporous ZSM-5 zeolites via alkali treatment for the direct hydroxylation of benzene to phenol with N_2O. *J. Catal.* **260**, 193–197. (doi:10.1016/j.jcat.2008.09.002)
26. Su LL, Zhang JQ, Wang HX, Li YG, Shen WJ, Xu YD, Bao XH. 2003 Creating mesopores in ZSM-5 zeolite by alkali treatment: a new way to enhance the catalytic performance of methane dehydroaromatization on Mo/HZSM-5 catalysts. *Catal. Lett.* **91**, 155–167. (doi:10.1023/B:CATL.0000007149.48132.5a)
27. Nie L, Yu J, Li X, Cheng B, Liu G, Jaroniec M. 2013 Enhanced performance of NaOH-Modified Pt/TiO_2 toward room temperature selective oxidation of formaldehyde. *Environ. Sci. Technol.* **47**, 2777–2783. (doi:10.1021/es3045949)
28. Mahshid S, Askari M, Ghamsari MS. 2007 Synthesis of TiO_2 nanoparticles byhydrolysis and peptization of titanium isopropoxide solution. *J. Mater. Process. Technol.* **189**, 296–300. (doi:10.1016/j.jmatprotec.2007.01.040)
29. Yoldas BE. 1986 Hydrolysis of titanium alkoxide and effects of hydrolytic polycondensation parameters. *J. Mater. Sci.* **21**, 1087–1092. (doi:10.1007/BF01117399)
30. Niu L, Zhang Q, Liu J, Qian J, Zhou X. 2016 TiO_2 nanoparticles embedded in hollow cube with highly exposed {001} facets: facile synthesis and photovoltaic appli*cations*. *J. Alloys Compd.* **656**, 863–870. (doi:10.1016/j.jallcom.2015.10.039)
31. Hou C, Liu W, Zhu J. 2017 Synthesis of NaOH-Modified $TiOF_2$ and its enhanced visible light photocatalytic performance on RhB. *Catalysts* **7**, 243. (doi:10.3390/catal7080243)
32. Hou C, Zhu J, Song Q. 2018 Low temperature synthesis of nest-like microsphere with exposed (001) facets and its enhanced photocatalytic performance by NaOH alkalization. *Catalysts* **8**, 70. (doi:10.3390/catal8020070)
33. Li G, Li L, Boerio-Goates J, Woodfield BF. 2005 High purity anatase TiO_2 Nanocrystals: near room-temperature synthesis, grain growth kinetics, and surface hydration chemistry. *J. Am. Chem. Soc.* **127**, 8659–8666. (doi:10.1021/ja050517g)
34. Li W, Body M, Legein C, Dambournet D. 2017 Identify OH groups in $TiOF_2$ and their impact on the lithium intercalation properties. *J. Solid State Chem.* **246**, 113–118. (doi:10.1016/j.jssc.2016.11.010)
35. Iwata T, Watanabe A, Iseki M, Watanabe M, Kandor H. 2011 Strong donation of the hydrogen bond of tyrosine during photoactivation of the BLUF domain. *J. Phys. Chem. Lett.* **2**, 1015–1019. (doi:10.1021/jz2003974)

36. Yongcheng N. 2000 Structural identification of organic compounds and organic spectroscopy. Science Press. (http://as.wiley.com/WileyCDA/WileyTitle/productCd-3527312404.html)
37. Lv K, Xiang Q, Yu J. 2011 Effect of calcination temperature on morphology and photocatalytic activity of anatase TiO_2 nanosheets with exposed {001} facets. *Appl. Catal. B Environ.* **104**, 275–281. (doi:10.1016/j.apcatb.2011.03.019)
38. Park H, Choi W. 2004 Effects of TiO_2 surface fluorination on photocatalytic reactions and photoelectrochemical behaviors. *J. Phys. Chem. B* **108**, 4086–4093. (doi:10.1021/jp036735i)
39. Zhao J, Li W, Li X, Zhang X. 2017 Low temperature synthesis of water dispersible F-doped TiO_2 nanorods with enhanced photocatalytic activity. *RSC Adv.* **7**, 21 547–21 555. (doi:10.1039/c7ra00850c)
40. Cao X, Luo S, Liu C, Chen J. 2017 Synthesis of bentonite-supported Fe_2O_3-Doped TiO_2 superstructures for highly promoted photocatalytic activity and Ti recyclability. *Adv. Powder Technol.* **28**, 993–999. (doi:10.1016/j.apt.2017.01.003)
41. Wang B, Qi H, Liu Z, Jin Y, Wang H, Yuan J, Zhao J, Shao J. 2017 Structure, chemical state and photocatalytic activity of TiO_{2-x} nanostructured thin films by glancing angle deposition technique. *J. Alloys Compd.* **716**, 299–305. (doi:10.1016/j.jallcom.2017.05.041)
42. Wang H, Yi G, Tan M, Zu X, Luo H, Jiang X. 2015 Initial reactant controlled synthesis of double layered TiO_2 nanostructures and characterization of its spectra of absorption and photoluminescence. *Mater. Lett.* **148**, 5–8. (doi:10.1016/j.atlet.2015.02.011)
43. Yuan L, Weng B, Colmenares JC, Sun Y, Xu Y-J. 2017 Multichannel charge transfer and mechanistic insight in metal decorated 2D-2D Bi_2WO_6-TiO_2 cascade with enhanced photocatalytic performance. *Small* **13**, 1702253. (doi:10.1002/small.201702253)
44. Hu Y, Li D, Zheng Y, Chen W, He Y, Shao Y, Fu X, Xiao G. 2011 $BiVO_4$/TiO_2 nanocrystalline heterostructure: a wide spectrum responsive photocatalyst towards the highly efficient decomposition of gaseous benzene. *Appl. Catal. B* **104**, 30–36. (doi:10.1016/j.apcatb.2011.02.031)
45. Park H, Choi W. 2005 Photocatalytic reactivities of nafion-coated TiO_2 for the degradation of charged organic compounds under UV or visible light. *J. Phys. Chem. B* **109**, 11 667–11 674. (doi:10.1021/jp051222s)
46. Bera S, Rawal SB, Kim HJ, Lee WI. 2014 Novel coupled structures of $FeWO_4$/TiO_2 and $FeWO_4$/TiO_2/CdS designed for highly efficient visible-light photocatalysis. *ACS Appl. Mater. Interfaces* **6**, 9654–9663. (doi:10.1021/am502079x)
47. Yang C, Yu J, Li Q, Yu Y. 2017 Facile synthesis of monodisperse porous ZnO nanospheres for organic pollutant degradation under simulated sunlight irradiation: the effect of operational parameters. *Mater. Res. Bull.* **87**, 72–83. (doi:10.1016/j.materresbull.2016.11.024)
48. Yang C, Li Q, Tang L, Xin K, Bai A, Yu Y. 2015 Synthesis, photocatalytic activity, and photogenerated hydroxylradicals of monodisperse colloidal ZnO nanospheres. *Appl. Surf. Sci.* **357**, 1928–1938. (doi:10.1016/j.apsusc.2015.09.140)
49. Yuan L, Yang M-Q, Xu Y-J. 2014 Tuning the surface charge of graphene for self-assembly synthesis of a $SnNb_2O_6$ nanosheet–graphene (2D–2D) nanocomposite with enhanced visible light photoactivity. *Nanoscale* **6**, 6335–6345. (doi:10.1039/C4NR00116H)
50. Lin L, Huang M, Long L, Sun Z, Zheng W, Chen D. 2014 Fabrication ofathree-dimensional BiOBr/BiOI photocatalyst with enhanced visible light photocatalytic performance. *Ceram. Int.* **40**, 11 493–11 501. (doi:10.1016/j.ceramint.2014.03.039)